Cement & Concrete Composites 33 (2011) 936–948

Contents lists available at ScienceDirect

Cement & Concrete Composites

journal homepage: www.elsevier.com/locate/cemconcomp

A discrete element model of concrete under high triaxial loading

V.T. Tran [a], F.-V. Donzé [a,b,*], P. Marin [a]

[a] Laboratoire "Sols, Solides, Structures et Risques", UMR 5521, Université Joseph Fourier, Grenoble Université, Domaine Universitaire, B.P. 53, 38041 Grenoble cedex 9, France
[b] Earth Science and Resource Engineering, CSIRO, Queensland Centre for Advanced Technologies, 1 Technology Court, Pullenvale 4069, Australia

ARTICLE INFO

Article history:
Received 3 June 2010
Received in revised form 1 December 2010
Accepted 4 January 2011
Available online 13 January 2011

Keywords:
Discrete Element Method
Cohesive granular geomaterials
Concrete
Triaxial compressive tests
High confining pressure

ABSTRACT

A numerical model based on a three dimensional Discrete Element Method (DEM) has been used to study the behavior of concrete under high-confining pressures (up to 650 MPa). At this range of pressures, irreversible compaction of the material occurs and needs to be considered. Within the discontinuous nature of the model, a local constitutive law has been developed to reproduce this phenomenon quantitatively. Local parameters to be used in this constitutive law are identified by simulating reference uniaxial and triaxial experimental tests in compression. Once these parameters have been obtained, the model is used to predict the response of concrete sample for triaxial compressive tests at different levels of confinement. Beyond the macroscopic volumetric and stress–strain response, the model gives interesting insights on the local evolution of the nature of the interaction forces between the discrete elements. The computational implementation has been carried out in the discrete element and open source code YADE (http://yade-dem.org [20]).

1. Introduction

Concrete is a building material used for sensitive infrastructures like nuclear power reactors. However its behavior remains partially unknown under extreme loading, such as explosions or ballistic impacts [8,26,27]. This is due to the difficulty of reproducing experimentally such a loading and the intrinsic complexity of concrete behavior [12]. Predicting its response under dynamic loading first needs the experimental characterization of its static behavior in compression under very high confinement, where different damage modes, which strongly depend on stress state and loading path, occur. Among these modes, the principal ones to be well understood are the phenomena of brittle damage and irreversible strain such as compaction. Most of the available experimental results in literature only relate to triaxial loadings with moderate confining pressure [21]. In these, only the transition from a brittle to a ductile behavior which is characteristic of cohesive materials, is well understood. To go further, experimental studies on the triaxial behavior of cementitious materials were carried out at higher confining pressures but they were limited to small mortar samples [2,5,18]. Recently, a triaxial press of high capacity has been used to characterize the triaxial behavior of concrete under various loading paths [13,25,30]: Hydrostatic, triaxial, proportional and oedometric tests were performed at high-confining pressure (up to one GigaPascal). The triaxial and proportional tests showed the existence of strain limit states, defining a limit state threshold independent of the loading path. These tests, which represent a major breakthrough in studying concrete material at the decimetric scale, will be used to calibrate and validate the present numerical model.

The complex constitutive behavior of concrete, arising from extensive micro-cracking and macro-cracking, is difficult to characterize in terms of a continuum formulation [4]. An alternative to the classical continuous numerical approaches is to use discrete-based methods which represent the material as an assemblage of independent elements, interacting with one another. The model then explicitly reproduces the discrete nature of the discontinuities, which are represented as the boundary of each element. The discrete models, are often applied to investigate the mechanical behavior of frictional cohesive materials, by assuming that they can be approximated as assemblies of discrete elements bonded together by different models of cohesive forces or cementation effects; the overall mechanical behavior can be evaluated through the collective contributions of these discrete elements under loading or unloading processes exhibiting motion, displacement, sliding, inter-element rotation. In addition the nucleation of cracks is mimicked by de-bonding of elements [23]. Thus, discrete models [6,7,9–11], which directly take into consideration the physical mechanisms and the influence of the concrete aggregate structure, offer an interesting alternative tool to model fracture in concrete, since this method does not rely upon any assumption about where and how a crack or several cracks occur and propagate as the medium is naturally discontinuous.

* Corresponding author at: Laboratoire "Sols, Solides, Structures et Risques", UMR 5521, Université Joseph Fourier, Grenoble Université, Domaine Universitaire, B.P. 53, 38041 Grenoble cedex 9, France.
E-mail address: donze@geo.hmg.inpg.fr (F.-V. Donzé).

0958-9465/$ - see front matter Crown Copyright © 2011 Published by Elsevier Ltd. All rights reserved.
doi:10.1016/j.cemconcomp.2011.01.003

When using the DEM to represent a real concrete sample, the local constitutive parameters are assigned to each of the interaction forces between the elements, such that the macroscopic behavior of the entire set of discrete elements is representative of the real material at the macro-scale. To assign the values of the local constitutive parameters, a calibration procedure can be used [3,15,16,29]. It is generally based on the simulation of quasi-static uniaxial and triaxial compression/traction tests. For example, a compression test model was developed [26] in YADE [19] for a standard-sized specimen, with the following characteristics:

- a compact, polydisperse discrete element set is generated,
- an elastic compression test is run with local elastic parameters given by the "macro–micro" relations [16],
- compressive rupture axial tests are simulated to deduce the plastic local parameters.

The main purpose of this paper is to present a model based on a three dimensional Discrete Element Method (DEM), able to reproduce the behavior of concrete under a high-confining pressure (up to 650 MPa). Using solely local elastic–brittle or even elastic–perfectly plastic constitutive laws, as generally formulated in common DEM codes, is not sufficient to reproduce quantitatively the behavior of concrete for high confinement loadings. At this range of pressures, irreversible compaction of the material occurs and needs to be considered. This is why a specific interaction law has been developed here to reproduce this phenomenon quantitatively.

After presenting the numerical model in Section 1, the experimental tests on concrete that were carried out with a high confinement [13,28] are presented in Section 2. Their results will be used as a reference case to compare with the results of the present model. The identification of the parameters of the model is first done in Section 3. Thereafter, the values of these local parameters are set up using uniaxial compressive–tensile tests, a hydrostatic test at 650 MPa and a triaxial test carried out at 50 MPa. Once calibrated, the model has been used to predict the concrete sample's responses for higher confining pressures. The maximum confining pressure considered was 650 MPa. Finally, the local properties of the model are discussed.

2. Discrete element model

There are different Discrete Element Methods [11] applied in the Geotechnical field, and we will use in this work the classical Discrete (or Distinct) Element Method formulation (DEM) pioneered by Cundall and Strack [7]. Basically, the algorithm involves two steps. In the first one, interaction forces are computed when elements slightly interpenetrate each other: this force–displacement formulation is often referred to as a Smooth contact method or also as the Force–Displacement method. In the second step, Newton's second law is used to determine, for each discrete element (DE), the resulting acceleration, which is then time integrated to find the new element positions. This process is repeated until the simulation is finished. This simultaneous numerical solution of the system is also known as the Molecular Dynamics (MD) formalism.

2.1. MD formulation

For small deformations, cohesive frictional geomaterials exhibit a linear elastic response. To reproduce this behavior, linear elastic interaction forces between the discrete elements are sufficient and lead to small simulation times. In the present model, the initial elastic interaction force, which represents the action of element a on element b, does not only involve elements in contact, but elements which are also separated by a distance smaller than an interaction radius controlled by a ratio γ defined by,

$$\gamma(R_a + R_b) \geqslant D_{ab} \tag{1}$$

where D_{ab} is the distance between the centroids of elements a and b, R_a and R_b are the radii of elements a and b and $\gamma \geqslant 1$ respectively . This is an important difference from classical Discrete Element Methods which use spherical elements where only contact interactions are considered ($\gamma = 1$).

This choice was made so that the average number of interactions per DE equals 12. By setting such a ratio, the macroscopic Young's modulus which depends on the local stiffnesses is controlled more easily (see [9,10,15,24] for more details). However, this mid-range interaction is limited to nearest neighbors.

This model uses spherical discrete elements of individual radius and mass and two types of interactions are defined. The first ones are the initial interactions which are "bounding" interactions i.e., linear in tension and compression with a limit threshold. The second ones are purely linear repulsive and are created only when a new contact (i.e. $\gamma = 1$), occurs during the simulation.

Thus, the initial interaction force vector F which represents the action of DE a on DE b may be decomposed into a normal force vector F_n and a shear force vector F_s (see Fig. 1) which may be classically linked to relative normal and incremental shear displacements respectively, through the stiffnesses, K_n in the normal direction and K_s in the tangential direction [14].

The normal interaction force can be calculated through the updated local constitutive law, which is shown in Fig. 2, and can be split into two parts, the compressive and the tensile components. In the compressive part, the concrete's response is linear and the normal interaction force is given by:

$$F_n = K_n(D_{eq} - D_{ab}) \tag{2}$$

where F_n is the normal interaction force, D_{eq} and D_{ab} are the initial and current distances between two DE a and b respectively.

In the tensile part, the normal force can also be computed with Eq. (2). However, the stiffness may be modified by a softening factor ζ while the softening behavior occurs after the normal force has reached its maximum value, $F_{n,\max}$, which is calculated by Eq. (7). Therefore, the normal force is now calculated such that,

$$F_n = (D_{ab} - D_{rupture})\frac{K_n}{\zeta} \tag{3}$$

When the rupture occurs ($D_{ab} > D_{rupture}$), the interaction force is set to zero.

The shear force vector $\mathbf{F}_s$ is calculated by updating its orientation which depends on the orientation of the direction passing

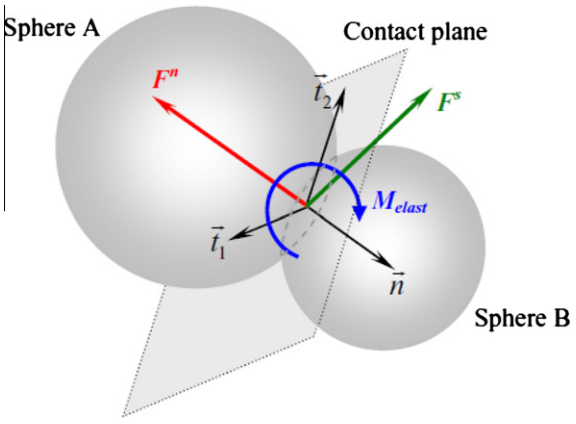

Fig. 1. Interaction between the DE.

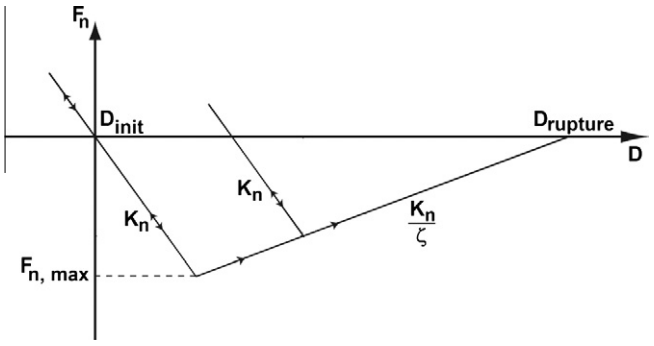

Fig. 2. Interaction laws in traction.

through the two centrods of the interacting DE, and by adding the increment $\Delta\mathbf{F}_s$ [14], which is defined by

$$\Delta\mathbf{F}_s = K_s\Delta\mathbf{U}_s \tag{4}$$

where $\Delta\mathbf{U}_s$ is the incremental shear displacement vector between the locations of the interacting points of the two elements over a timestep Δt.

Note that the stiffnesses used here depend on the macroscopic elastic property and the size of the elements and can be expressed as,

$$K_n = \alpha * E * R_{avg} \tag{5}$$

$$K_s = \beta * K_n \tag{6}$$

where α and β are dimensionless coefficients, E is Young's modulus, which is set here using the value obtained by a compressive experiment test [13] and R_{avg} is the average radius of two interacting elements.

To model the nonlinear behavior of the concrete material, a modified Mohr–Coulomb model has been used (see Fig. 3). For a given interaction, the maximum normal force $F_{n,\max}$ is defined as a function of tensile strength T. The maximum shear interaction force is characterized by the normal force F_n, the cohesion C, the contact friction angle Φ_c and the internal friction angle Φ_i. Therefore, the maximum normal force can be defined as,

$$F_{n,\max} = -TA_{\text{int}} \tag{7}$$

where $A_{\text{int}} = \pi(\min(R_a, R_b))^2$ is defined as the interacting surface. The maximum shear force is calculated for a link interaction, such that

$$F_{s,\max} = F_n \tan\Phi_i + CA_{\text{int}} \tag{8}$$

and when the new contacts appear during the simulation, their maximum shear force will only be frictional,

$$F_{s,\max} = F_n \tan\Phi_c \tag{9}$$

To reproduce quantitatively the behavior of a granular material when spherical discrete elements are used, the interaction between DE must transmit a moment [1,17,22] which controls the rolling occurring during shear displacement. Doing so, the sliding process increases and the resulting friction angle can reach values corresponding to those measured for concrete materials. This moment transferred between two elements in interaction can be written as,

$$M_{elast} = \sum \theta_r * K_r \tag{10}$$

where θ_r is the relative rotation angle and K_r is the rotational stiffness.

An elastic limit is introduced and when it is reached, a plastic moment defined by,

$$M_{plast} = \eta * F_n * R_{avg} \tag{11}$$

will take place (see Fig. 4). Here, η is a dimensionless factor used for the plastic moment, F_n is the normal interaction force and R_{avg} is the average radius of two interacting DE.

2.2. Updating the local constitutive law

We now propose in this work a more complete formulation of F_n in order to take into account the compaction process which occurs at a lower scale than the discretization size of the model. In this formulation,the concrete's response in compression is first linear (section AB in Fig. 5) and the normal interaction force is given by Eq. (2). Then, when the interaction's deformation reaches an elastic deformation limit $\varepsilon_{\max}$ which is related to the interaction distance (D_1), a hardening-damage response is considered (section BC). At this step of the interaction, the normal interaction force is characterized by a nonlinear stiffness K_{n2}, which is an exponential function of the deformation and controlled by three parameters ζ_1, ζ_2 and ζ_3. This stiffness is expressed as,

$$K_{n2} = K_n\left[\zeta_1\left(e^{\zeta_2*(\varepsilon-\varepsilon_{\max})}\right) + \zeta_3\right] \tag{12}$$

where maximum elastic deformation is defined by,

$$\varepsilon_{\max} = \frac{D_{eq} - D_1}{D_{eq}} \tag{13}$$

Finally, the complete normal interaction force is expressed as,

$$F_n = K_n(D_{eq} - D_1) + K_{n2}(D_1 - D_{ab}) \tag{14}$$

The nonlinear part of the stiffness has been added to be in agreement with the experimental results obtained by triaxial tests under high confinement [13]. In fact, the parameter ζ_3 controls the slope of the beginning part of the nonlinear behavior, whereas the sum $\zeta_1 + \zeta_3$ controls the slope of the last part of this nonlinear behavior. The parameter ζ_2 controls the curvature of the compaction's curve.

To increase the lateral deformation which plays a major role in the contraction–dilatancy transition of the volumetric behavior

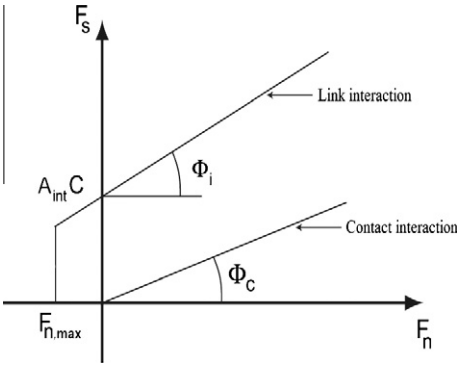

Fig. 3. Modified Mohr–Coulomb criterion.

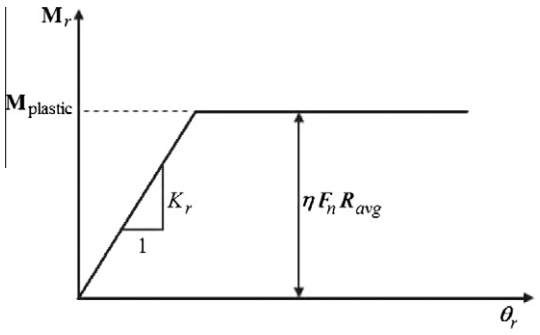

Fig. 4. Rolling moment law considered between interacting DE.

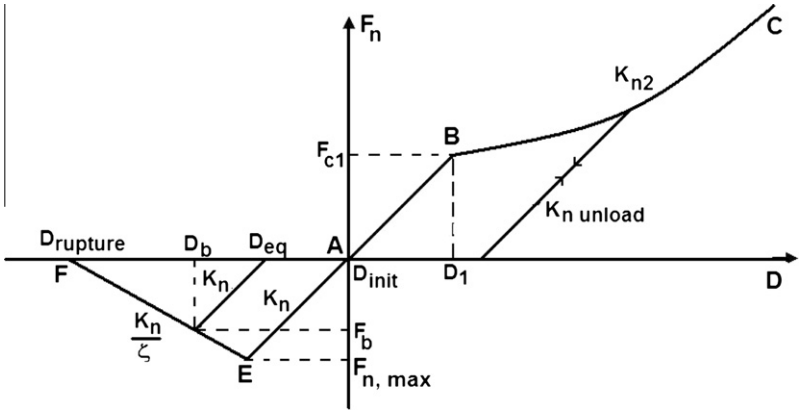

Fig. 5. Summary of the constitutive law.

(Fig. 8), a coefficient λ has been added to the modified Mohr–Coulomb rupture criterion. This coefficient controls the sliding threshold of the link interaction (Fig. 6). It will be calibrated to ensure that the sliding mode is activated as soon as possible. Thus, the maximum shear force of the "link" type interaction is defined as,

$$F_{s,\max} = F_n \tan \Phi_i + CA_{\text{int}} \quad \text{if } F_n \tan \Phi_i < (\lambda - 1) * CA_{\text{int}} \tag{15}$$

$$F_{s,\max} = \lambda CA_{\text{int}} \quad \text{if } F_n \tan \Phi_i \geqslant (\lambda - 1) * CA_{\text{int}} \tag{16}$$

Based on the physical model given in this section, a complete mechanical model is composed of normal, tangential and rolling contact components, as shown in Fig. 7.

3. Experimental triaxial compressive tests

Recent high-confining pressure triaxial compressive tests on concrete specimens have been carried out by Gabet et al. [13]. The concrete material used to build up the samples, has a mean strength of 30 MPa in compression, a Young's modulus of 25 GPa, a Poisson's ratio of 0.21, and a porosity of 12%. Its Young's modulus and Poisson's ratio can be directly used to set up the elastic part of the numerical model (see Eqs. (5) and (6)). The experimental samples are cylinders with a height of 0.14 m and a diameter of 0.07 m. The results of these experiments will be used as reference cases to validate the present numerical model. The experimental result of a hydrostatic test carried out up to 500 MPa is presented in Fig. 8c, where an important compaction process is observed. The slope of the strain–stress curve first decreases before it increases, because of the relative importance of the irreversible deformation processes observed during concrete compaction. The volumetric behavior curves in Fig. 8b show that a transition contraction–dilatancy occurs during the loading path (except for the 500 MPa test, where specific experimental conditions could be evoked), which is a threshold of the volumetric deformation where the compaction process will be replaced by a dilatancy (see Fig. 8d). This contraction–dilatancy transition is frequently observed for concrete during triaxial tests.

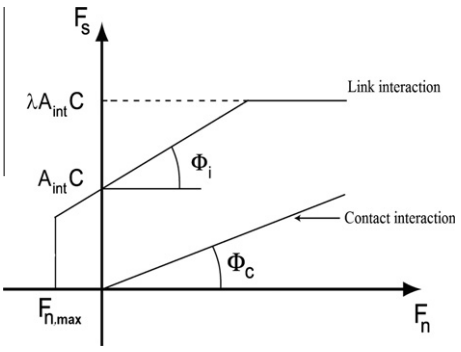

Fig. 6. Rupture criterion used in the model.

4. Numerical simulations

The numerical model has been set up to simulate the experimental tests presented previously. Hence, the local parameters of the model were first identified using uniaxial compressive–tensile tests, hydrostatic tests at 650 MPa and the triaxial test carried out at 50 MPa. Once calibrated, the model will be used to predict the concrete sample's responses for the other confining pressures.

4.1. Numerical sample preparation and monitoring

The generated numerical samples are parallelepipeds (and not cylindrical as in the experiments, but one could expect that the geometry has a negligible effect on the results) of size 0.07 m × 0.14 m × 0.07 m. The number of DE in the numerical sample is about 10,000. The positions and diameters of the DE have been generated randomly. The size distribution obtained for the DE is shown in Fig. 9. The numerical compacity of the sample is about 0.53 (which is not comparable to the real geometry because the DE are spherical), but this value is high enough to represent a 3D dense packing of spheres set with a low range of distribution size. The isotropy of the numerical medium is verified by plotting the cumulative orientation distribution of interactions and it can be seen that this sample has a quasi-uniform distribution (see Fig. 10).

A numerical triaxial test is performed using the following protocol. First, the numerical sample is subjected to a hydrostatic confining pressure up to a pressure value p, by moving the surrounding plates (see Fig. 11). Once this pressure value is reached, the top and bottom plates are moved vertically as loading platens, using a force-controlled condition. During the loading of the test, the displacement of the lateral plates are controlled to maintain a constant confining pressure p. Note that, these numerical tests are carried out with frictionless lateral plates, similar to the experimental condition tests [13], in which a confining fluid is used. To be as close as possible to the experimental tests, a small friction value is considered between the sample and the loading platens in the numerical case. The axial stress is computed by dividing the total axial force applied to the top plate by its surface and the deformations are computed via the movement of the plates.

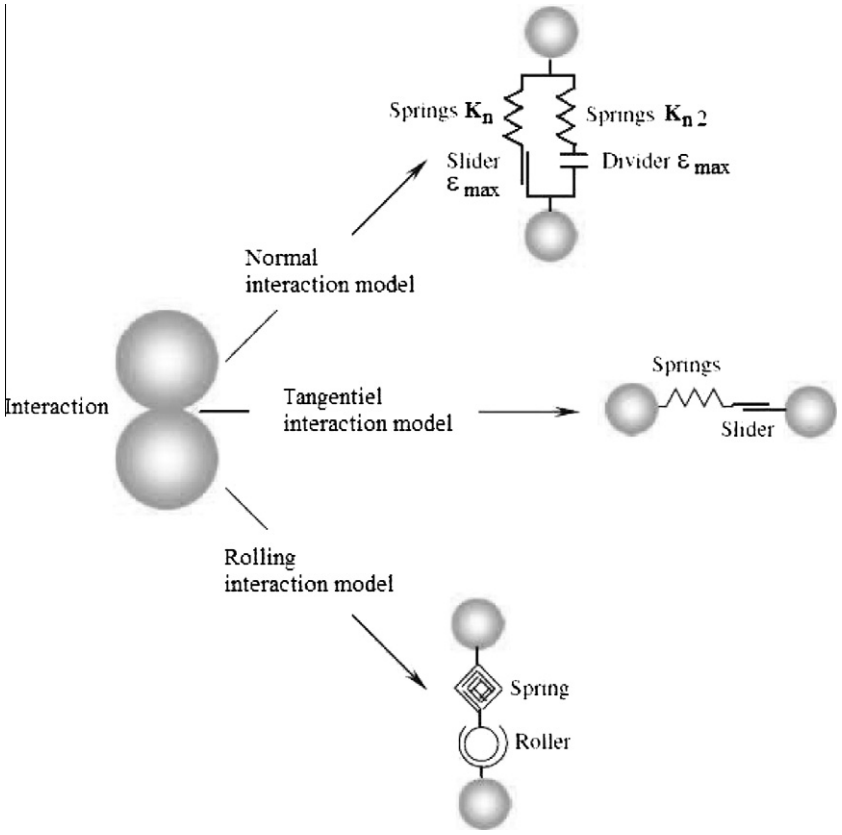

Fig. 7. Interaction model in the DEM with MTL (for the "link" type interaction).

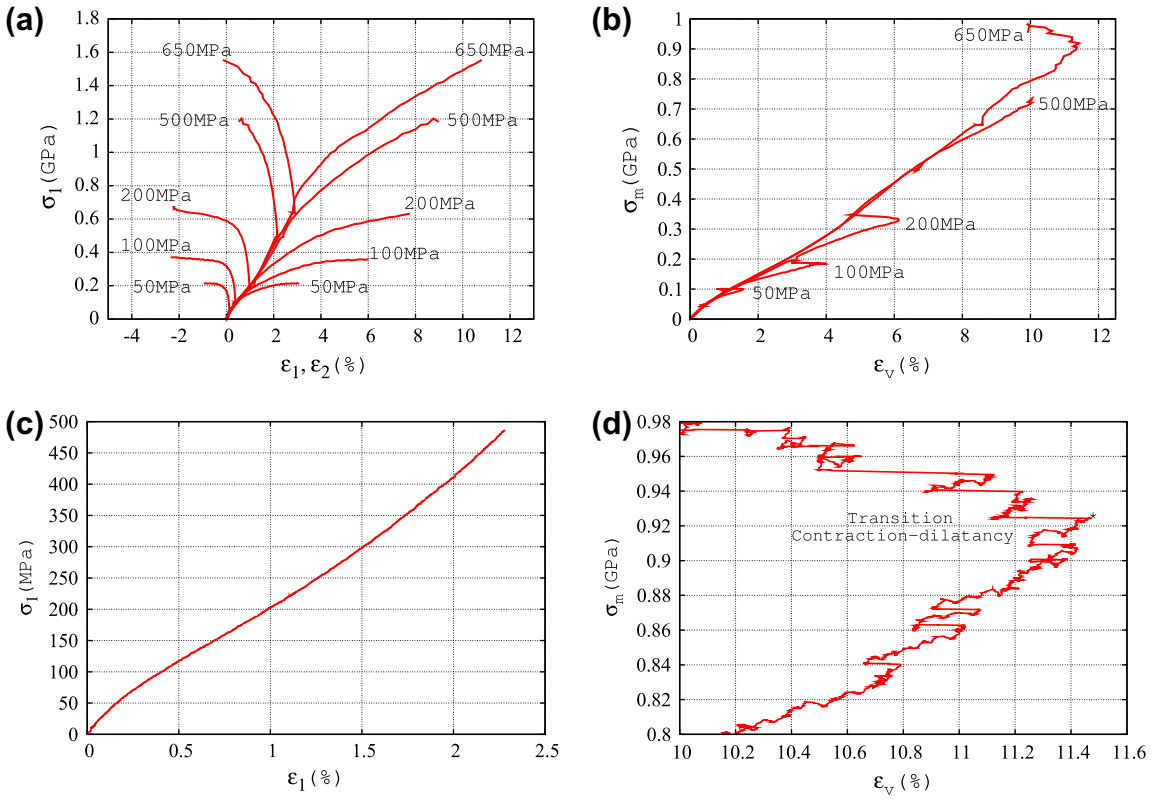

Fig. 8. Experimental stress–strain curves (a), volumetric deformation curves (b), hydrostatic curve up to 500 MPa (c) and a zoom on the volumetric deformation at 650 MPa (d) [13].

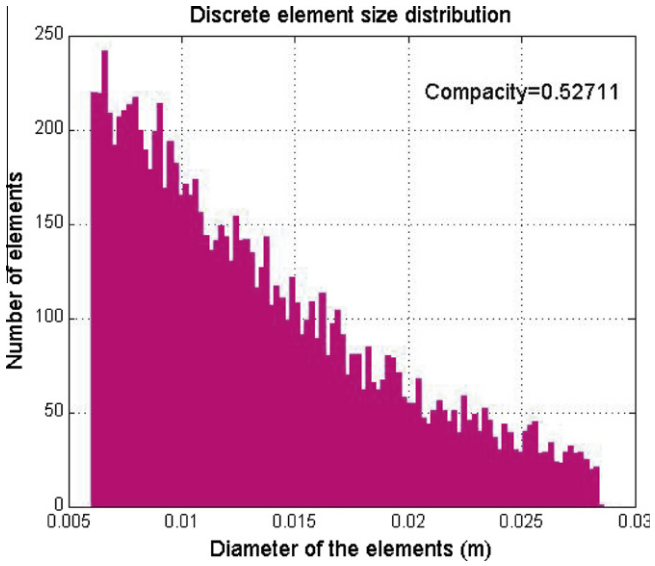

Fig. 9. Size distribution of the DE in the numerical sample.

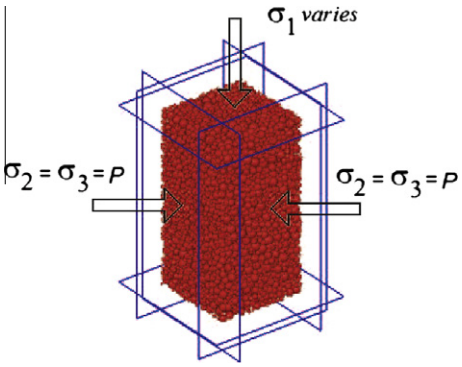

Fig. 11. Triaxial test configuration.

4.2. Calibration

The calibration of the model parameters is a necessary step to simulate quantitatively the behavior of a real geomaterial. It is conveniently done by comparing real and simulated reference tests. With these comparisons, the model parameters, such as the tensile strength T, the cohesion C, the softening factor ζ, the internal friction angles (Φ_i, Φ_c), the stiffnesses' coefficients (α, β, ζ_1, ζ_2, ζ_3), the maximum elastic deformation ε_{max} and the coefficient of maximum shear force λ, can be set up. The interaction range γ has been set by the geometry of the numerical sample and its value is 1.37. The identification procedure (which has already been developed in previous works [16,24]) is done through a group of reference tests which include, uniaxial compression–traction, 650 MPa hydrostatic and 50 MPa triaxial tests, described in the following subchapters.

4.2.1. Uniaxial compression–traction tests

The uniaxial compression–traction tests have been used to calibrate the following parameters α, β, C, ζ, T, Φ_i and Φ_c. First of all, the values of the linear stiffness coefficients, α and β, were selected to match Young's modulus and Poisson's ratio of the concrete material while all other parameters of the test were kept constant with a sufficiently high value to respect a purely elastic response of the model. The Young's modulus and the Poisson's ratio values correspond to the initial slope of the stress–strain diagram and the ratio lateral–axial strain with a maximum axial strain of 0.1%.

σ_t of the uniaxial tensile test was used to obtain the values of the local tensile strength T and the softening coefficient ζ. Similarly, σ_c of the compressive test was used for the values of the cohesion C, the friction angles Φ_i and Φ_c. By doing so, the numerical and experimental results for the tensile and compressive tests show quite a good agreement (see Fig. 12, where the axial stress σ_1 versus the axial strain ε_1 and the lateral strain ε_2 are plotted).

4.2.2. Hydrostatic test at 650 MPa

The uniaxial compression test is not sufficient to calibrate the full irreversible response of the model, which is also characterized by the three hardening stiffness ratios ζ_1, ζ_2, ζ_3 and the maximum elastic deformation ε_{max}. This is why an experimental hydrostatic test performed at a confining pressure reaching 650 MPa, was used. With this hydrostatic test, it was possible to obtain information on the compaction process of the concrete material as well as evaluate its quantitative contribution. To show the importance of having an elastic-hardening constitutive law in the model, the experimental results are compared, first to numerical results obtained with this law and second with those obtained with a solely elastic constitutive law in compression. The use of the solely linear elastic law (see Fig. 13) shows a totally unrealistic linear increase

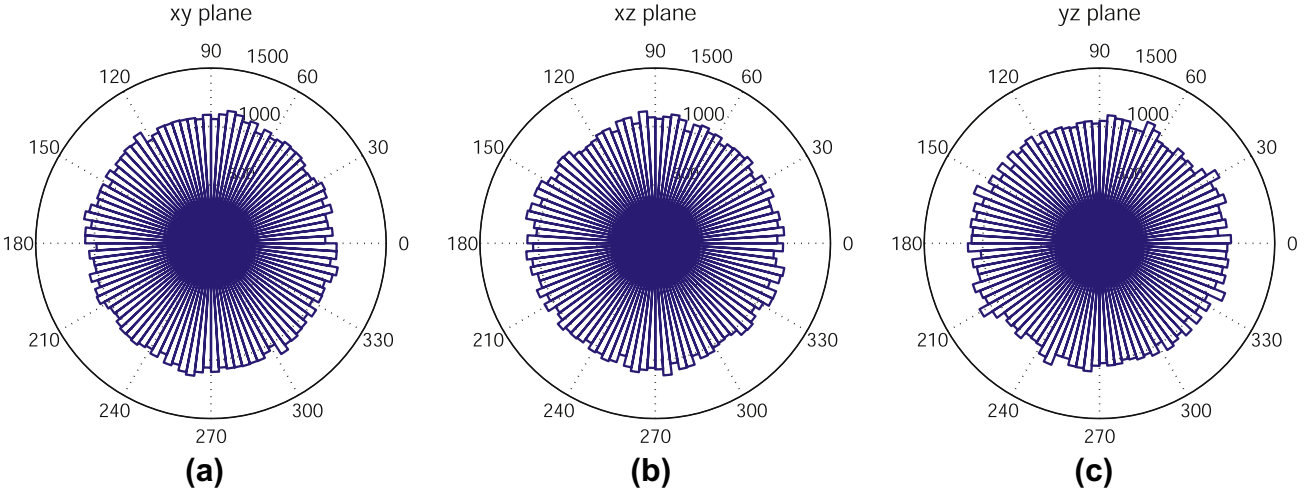

Fig. 10. Initial distribution of the interaction links' orientations in the numerical sample.

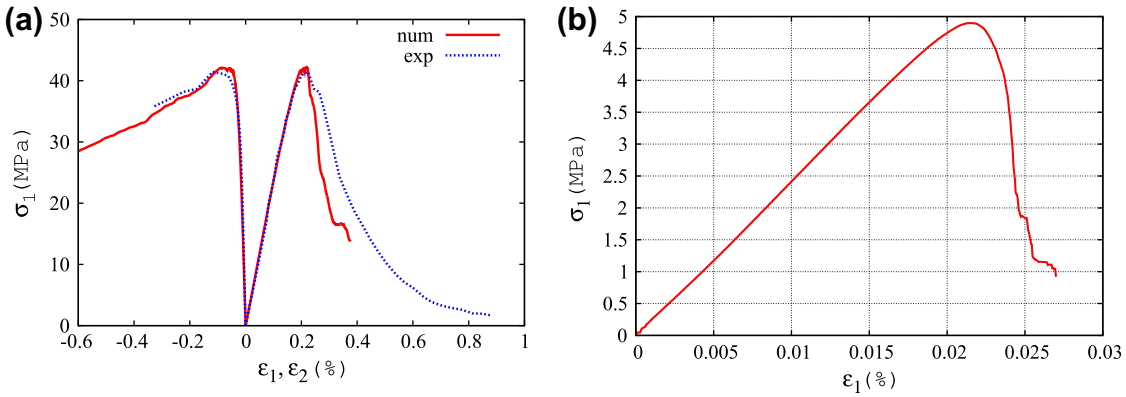

Fig. 12. Stress–strain curves for uniaxial compressive test (a) and tensile test (b). Solid and dotted lines correspond to the numerical and experimental results, respectively.

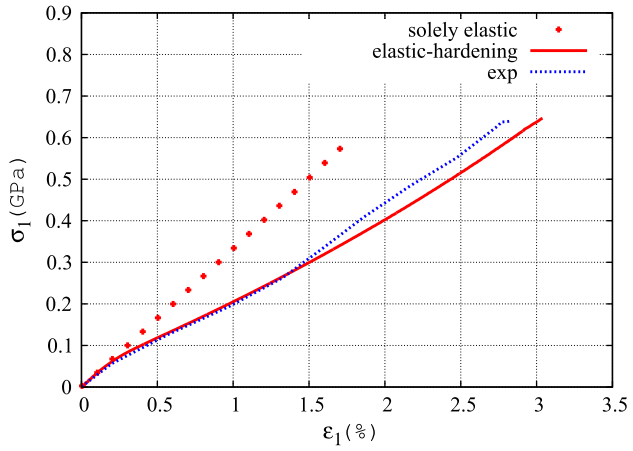

Fig. 13. Stress–strain curves for hydrostatic tests at 650 MPa of confining pressure. The solid and double-dotted lines represent the numerical results and the single-dotted line represents the experimental results.

of the axial stress versus the axial strain as soon as the axial strain exceeds 0.2%. Note that at this strain value, the maximum value of the elastic deformation ε_{max} is reached. When using the local elastic-hardening constitutive law, the results of the model fit the experimental results (solid line in Fig. 13). From the experimental curve, the parameter ζ_3 and the sum $\zeta_1 + \zeta_3$ were used to control the numerical slope from the beginning of the compaction phase (from 0.2% of axial strain) to the end of the hydrostatic phase. Moreover, parameter ζ_2 controls the curvature of this curve.(See Fig. 14)

4.2.3. Triaxial test at 50 MPa

The full 50 MPa triaxial test was used to finish the calibration process by fixing the value of the rupture criterion coefficient λ. This parameter controls the maximum shear force. When the lateral deformation decreases, a transition contraction–dilatancy is observed in the experiments (see Fig. 14). This volumetric transition is well reproduced by the model when choosing the right value for λ. Thus, the full elastic-hardening constitutive law of the numerical model can reproduce quantitatively the experimental triaxial compressive test carried out by Gabet et al. [13].

Since the local parameters of the model have been calibrated, their values are given in Table 1.

Table 1
Local parameter values of the numerical model.

Parameters	Values
Coefficient α	1
Coefficient β	0.25
ε_{max} (%)	0.2
Tensile limit (MPa)	9
Cohesion C (MPa)	4
Softening ζ	5
Internal friction angles Φ_i and Φ_c (°)	30
Coefficient ζ_1	0.2
Coefficient ζ_2	16
Coefficient ζ_3	0.275
Coefficient λ	5

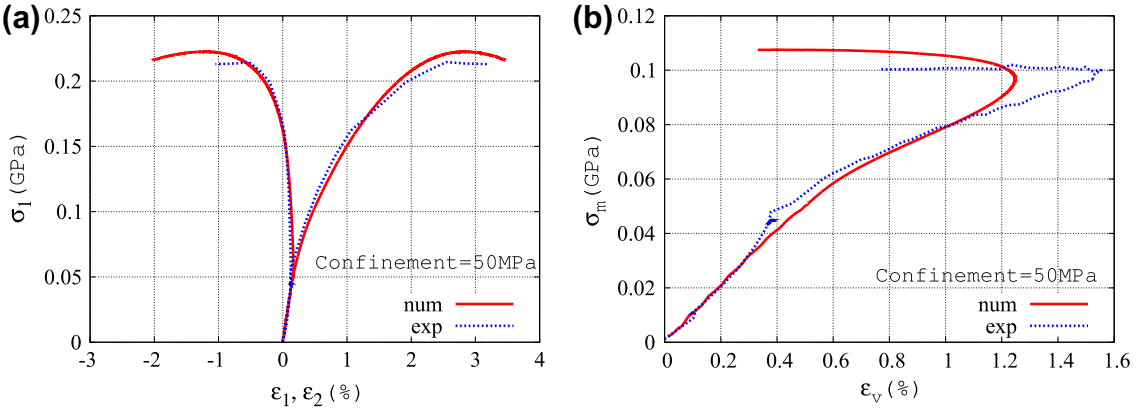

Fig. 14. Stress–strain curves at 50 MPa confining pressure. Solid and dotted lines represent the numerical and experimental results respectively.

4.3. Prediction for other confining pressures

The model parameters have been calibrated using uniaxial compressive–tensile, 650 MPa hydrostatic and 50 MPa triaxial tests. Without changing the values of these parameters, the numerical model is now used to simulate triaxial tests at other confining pressures. Four additional triaxial tests have been simulated for the following confining pressures: 100 MPa, 200 MPa, 500 MPa, 650 MPa. They are compared with data also available in the experimental campaign. For all these cases, the same initial numerical parallelepiped sample have been used. Both, experimental and numerical results are presented with lateral–axial strain/axial stress components and volumetric curves (see Fig. 15).

4.3.1. Strain–stress response of triaxial tests

The results indicate that in the hydrostatic phases,the numerical results are very close to the experimental measurements.

In the differential-stress phase, the simulated results are overall comparable with the experimental ones. Experimentally, for a 100 MPa test, a stagnation of the axial pressure is observed, without reaching a peak as is the case in the 50 MPa test. Still in the experiments, for the 200 MPa test, there is a decrease of the stiffness but without reaching a plateau as in the 100 MPa test. Then, for the 500 MPa and 650 MPa tests, the stiffness curves gradually decrease without changing slope. All the numerical curves show a stress peak and before it occurs, a decrease of the stiffness is observed in both the model and the experiments. The numerical and the experimental results differ in that the axial stress peaks are reached earlier in the numerical model than in the experiment. When adding friction on the lateral plates in the numerical model, this discrepancy tends to vanish. However, by doing so the elastic deformation is no longer homogeneous in the numerical sample. Thus, a clear explanation could not be obtained from the model, despite a large parametric study.

4.3.2. Volumetric behavior and limit state

As expected, the numerical and experimental volumetric deformations on the hydrostatic phase seem to fit very well (see Fig. 16). However, when the contraction–dilatation transition occurs at the same mean stress value, the amplitude of the maximum contraction of the numerical volumetric curves are lower than the experimental ones. This result is directly linked to the observations made on the stress–strain curve, and the conclusions are similar. Note, that in the 500 MPa experimental test, the results do not show a contraction–dilatancy transition because this test has been prematurely stopped.

Another way to deal with the contraction–dilatancy transition (also called the limit state), is to represent it in the (σ_m, q) stress space (see Fig. 17). Here again, the experimental and numerical results are in a very good agreement.

Thus, it can be concluded that the numerical model can reproduce macroscopic key properties such as the volumetric behavior of concrete during the hydrostatic phase and the contraction–dilatancy transition. We will now look at the evolution of the internal structure of the sample during its deformation.

4.4. Evolution of the internal structure of the sample

With the Discrete Element Method, it is possible to follow the evolution of the local properties of the sample during the simulation at the DE scale. For example, it is possible to track the values of the spatial distribution of the forces between the interacting

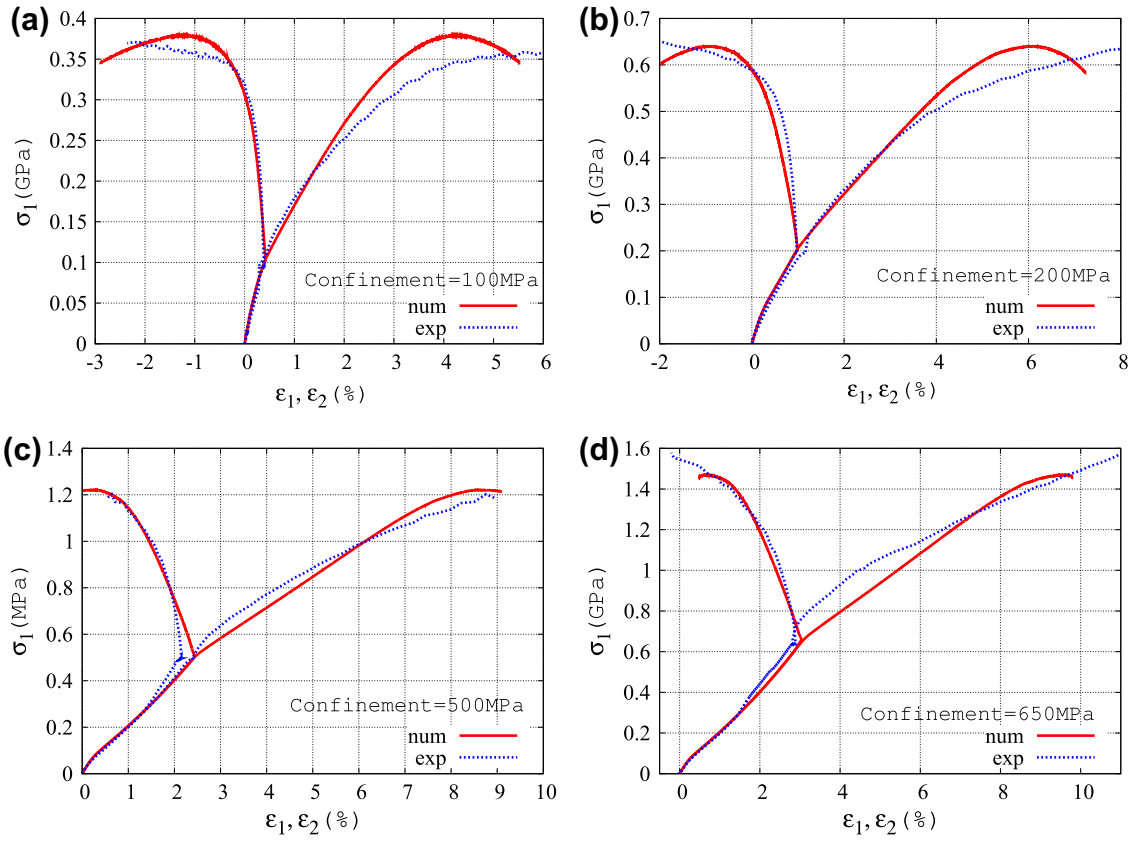

Fig. 15. Stress–strain curves for 100 MPa (a), 200 MPa (b), 500 MPa (c) and 650 MPa (d) confining pressures. Solid and dotted lines represent numerical and experimental results, respectively.

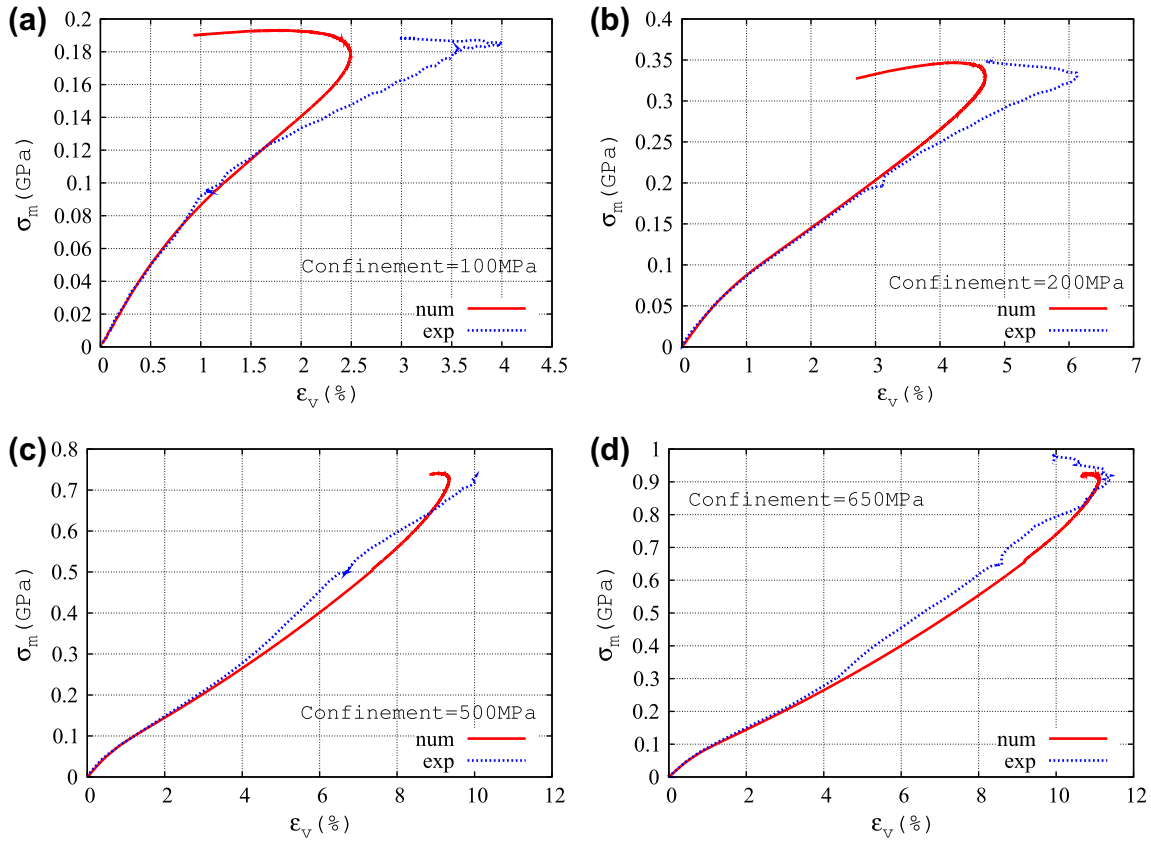

Fig. 16. Mean stress–volumetric strain curves for 100 MPa (a), 200 MPa (b), 500 MPa (c) and 650 MPa (d) confining pressures. Solid and dotted lines represent numerical and experimental results, respectively.

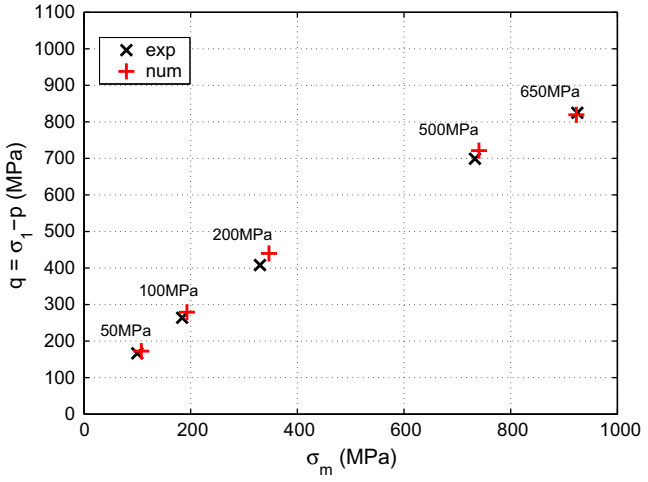

Fig. 17. Limit state points, defined as contraction–dilatancy transitions on the volumetric behavior curves for the experimental and numerical tests, are represented in the (σ_m, q) stress space.

discrete elements, the evolution of their interaction state or their displacements. What happens at the local scale during the transition from the brittle to the ductile response of the sample or how the compaction zones appear can be followed with the discrete model.

4.4.1. Brittle–ductile transition at low confining pressure

A very well known result is how the displacement of the DE evolves during a compressive test at low confining pressures (see [9] for example). A thin central vertical slice can be chosen to represent the displacement field occurring around the stress-peak region in the numerical sample (see Fig. 18a). It can be observed that the deformation is localized along narrow zones, delimiting cones. These failure patterns in compression seem consistent with the experimental observations (see Fig. 18b).

The distribution of interaction forces between elements can give information on the brittle failure mechanism. When considering a thin central vertical slice at the stress peak as in Fig. 19, the distribution of the tensile forces in (a), the linear step compressive forces in (b) and the nonlinear hardening step compressive forces in (c), show that the forces are mainly in an elastic regime. Note that the line width corresponds to the force magnitudes. Once the elastic tensile limit is reached, the links break and the interaction forces are no longer visible. It is also at this step that the deformation localizes. More details on this brittle process can be found in [23].

Finally, two different confining pressures (5 kPa and 5 MPa) were applied to the numerical sample and the evolution of the interaction force type was tracked during the simulation. When the confining pressure increases from 0 to 5 kPa, the number of interaction forces in traction and the number of broken links tends to decrease (see Fig. 20a and b), whereas the number of compressive forces in the linear step (section AB of the normal force law), strongly increases. Then, when the confining pressure increases from 5 kPa to 5 MPa, the number of compressive forces in the nonlinear hardening step (section BC of the normal force law) becomes more present (Fig. 20c). Here again, the number of interaction forces in traction dramatically decreases. This vanishing of the tensile forces and the stabilization of the number of broken links (visible on Fig. 21, when the confining pressure is higher than

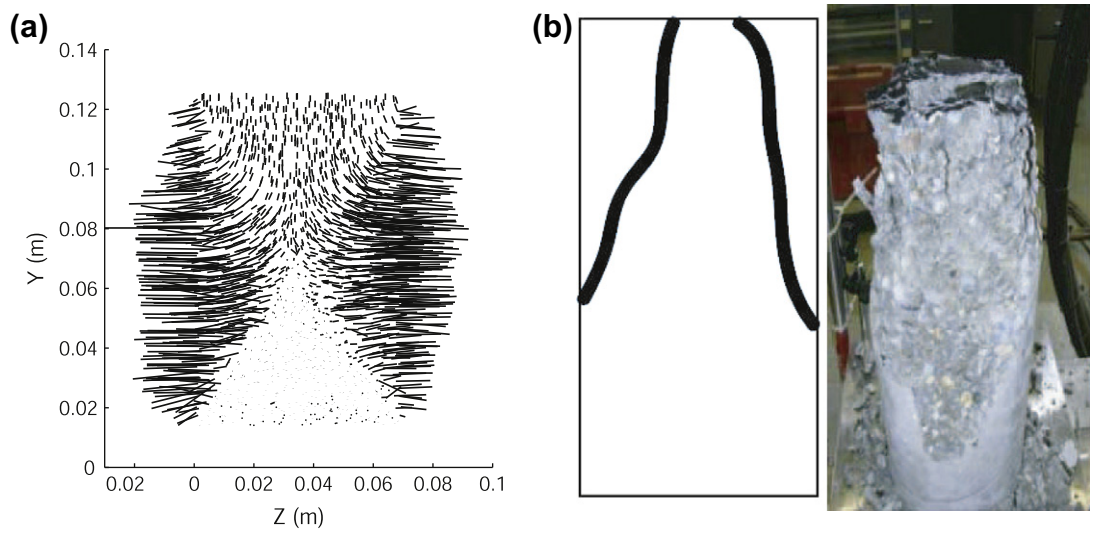

Fig. 18. Displacement field within a thin central vertical slice in the numerical sample around the peak stress state during a uniaxial compressive test (a), fracture topography of the experimental sample (b).

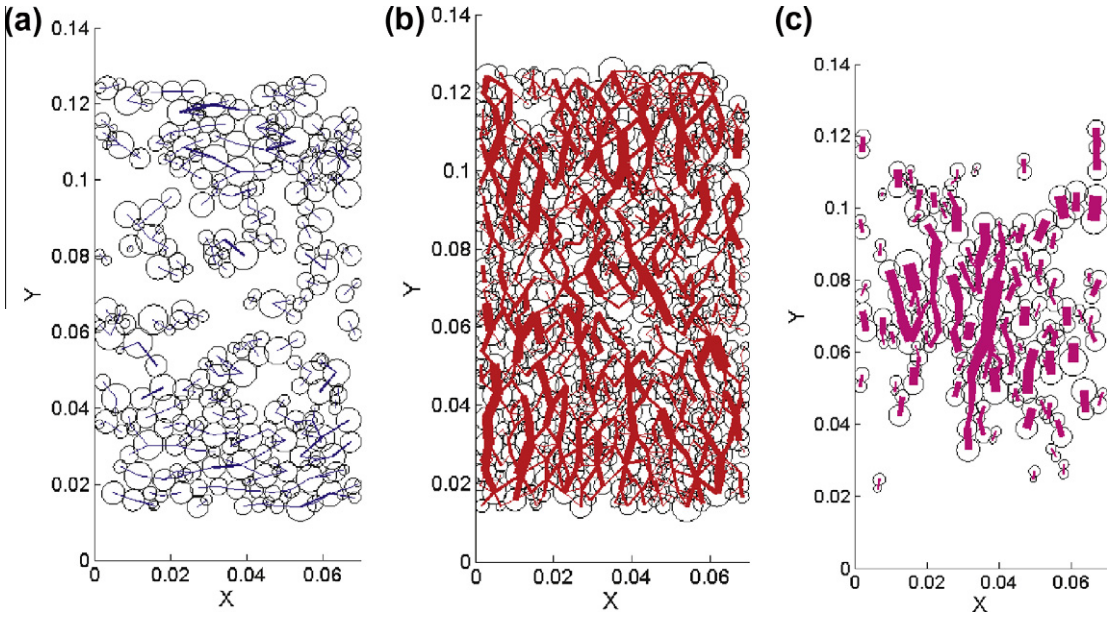

Fig. 19. Distribution of interaction forces in a thin central vertical slice in the numerical sample at the peak stress state during a uniaxial compressive test: tensile forces (a), forces in the linear compression step (b) and forces in the nonlinear hardening compression step (c).

100 MPa), corresponds to the transition from the brittle to the ductile behavior of the material, as observed at the macroscopic scale. When the confining pressure increases from 100 MPa to 650 MPa, the main state of the interaction forces corresponds to the nonlinear hardening step.

4.4.2. Nonlinearity in compression for high-confining pressures

When the confining pressure greatly increases, most of the interaction forces in the linear compressive state transfer to the nonlinear compressive state (i.e. hardening step) (Fig. 21). We can show that the interactions move from the linear state to the nonlinear state (i.e. hardening) at a rate which depends on the confining pressure. The number of interactions of the nonlinear state increases with the higher confining pressure whereas the tensile interactions disappear. Around the stress peak, the number of broken interactions decreases with an increase of the confining pressure. This redistribution of the type of existing forces, in compression, from a linear to a nonlinear state corresponds to the incoming compaction process.

Insight on how the compaction phenomenon and the resulting localization of the damage occur is gained by observing the evolution of the local interaction forces between discrete elements (see Fig. 22). When representing a thin vertical slice of the numerical sample at a 650 MPa confining pressure (see Fig. 22), it can be seen that very few interaction forces are in the tensile or linear compressive steps. Those that are, have a very low amplitude (Fig. 22a and b). On the other hand, most of the interaction forces in action are in the nonlinear compressive step and have high amplitudes. These forces are aligned in the main stress direction, i.e. the vertical one. Hence, the potential associated micro-cracking direction would be perpendicular to it, i.e. horizontal. This is what is indeed observed when the displacement field of the discrete

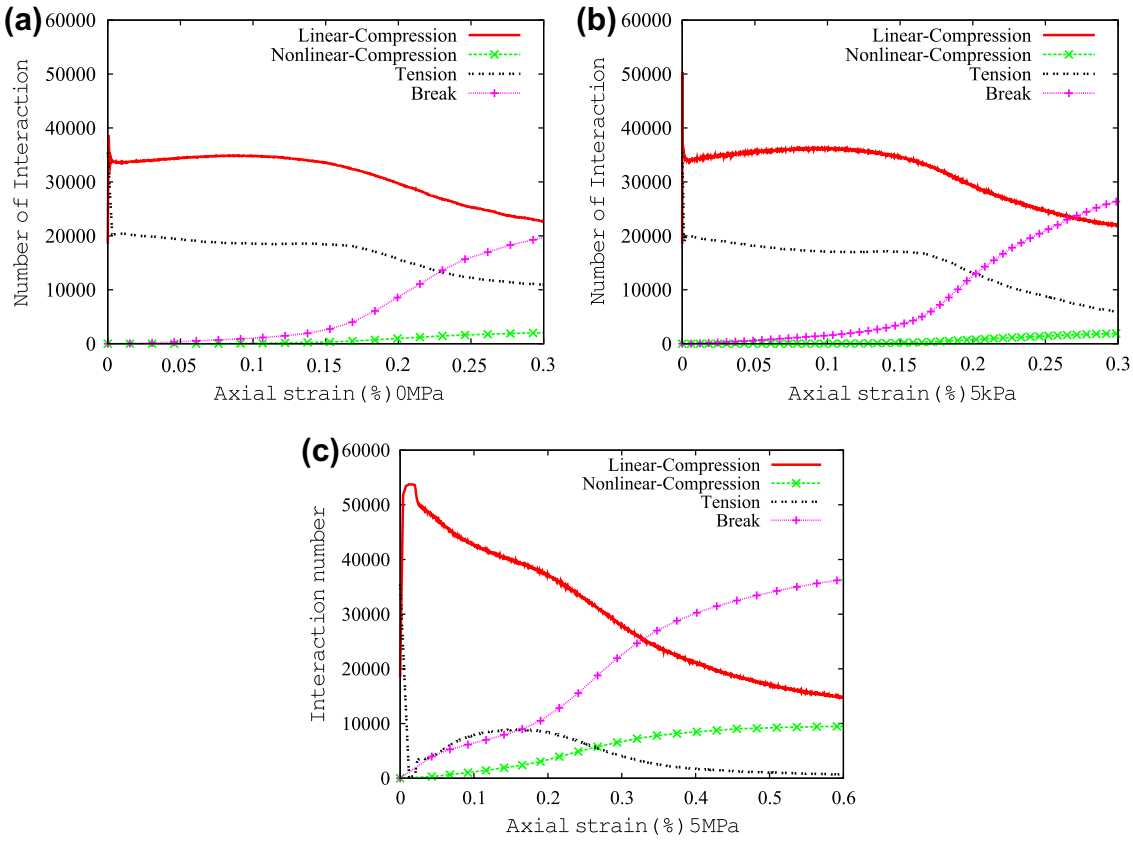

Fig. 20. Evolution of the number of interaction forces versus axial strain for different confining pressures: 0 Pa (a), 5 kPa (b) and 5 MPa (c). The different curves correspond to the nature of the interaction and the broken links.

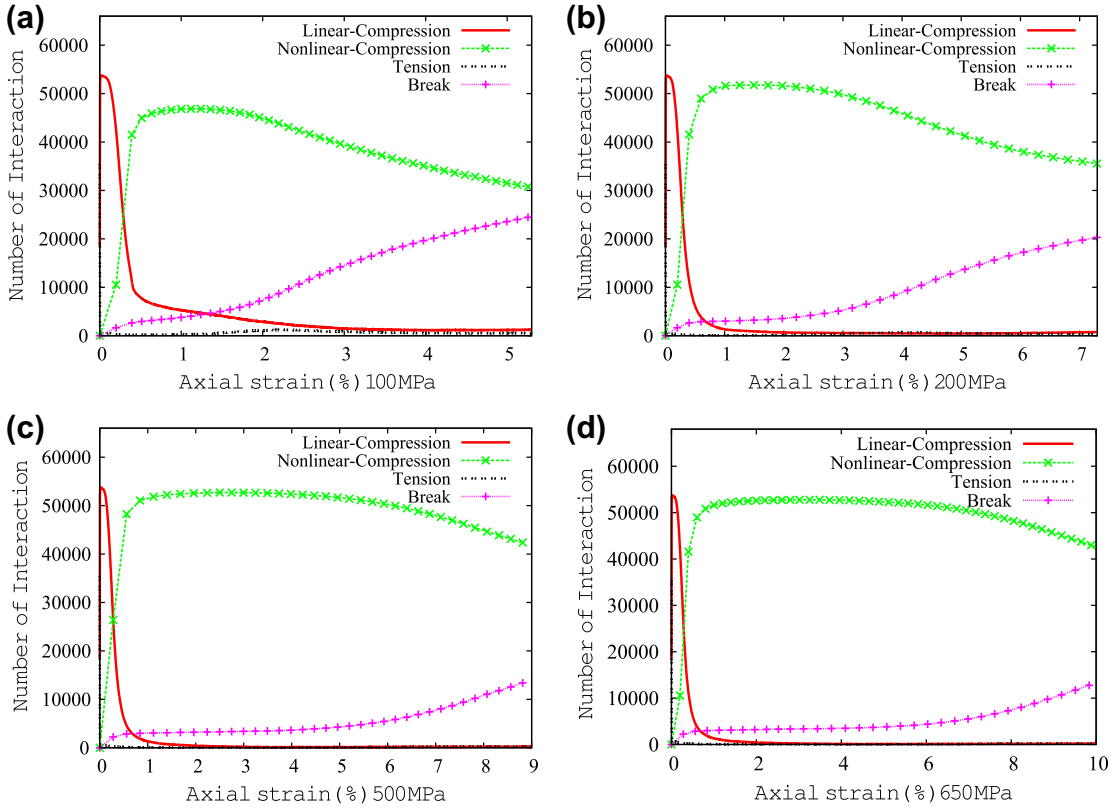

Fig. 21. Evolution of the number of interaction forces versus axial strain for different confining pressures: 100 MPa (a), 200 MPa (b), 500 MPa (c) and 650 MPa (d). The different curves correspond to the nature of the interaction and the broken links.

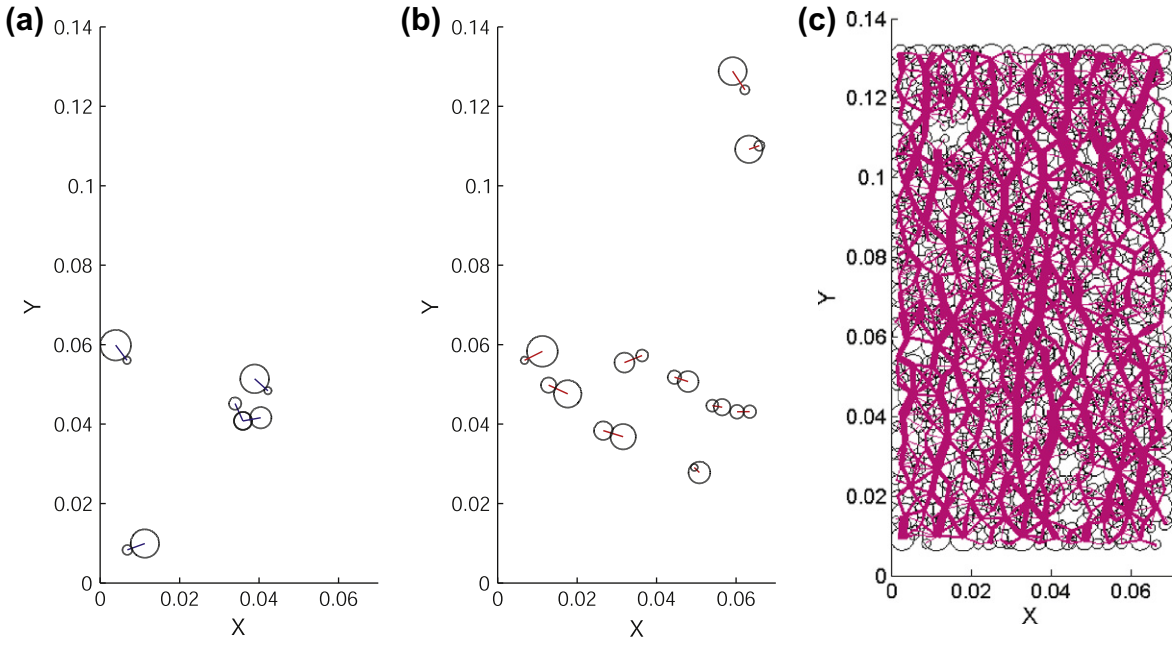

Fig. 22. Distribution of interaction forces for 650 MPa: traction (a), linear compression (b) and nonlinear (i.e. hardening) compression (c).

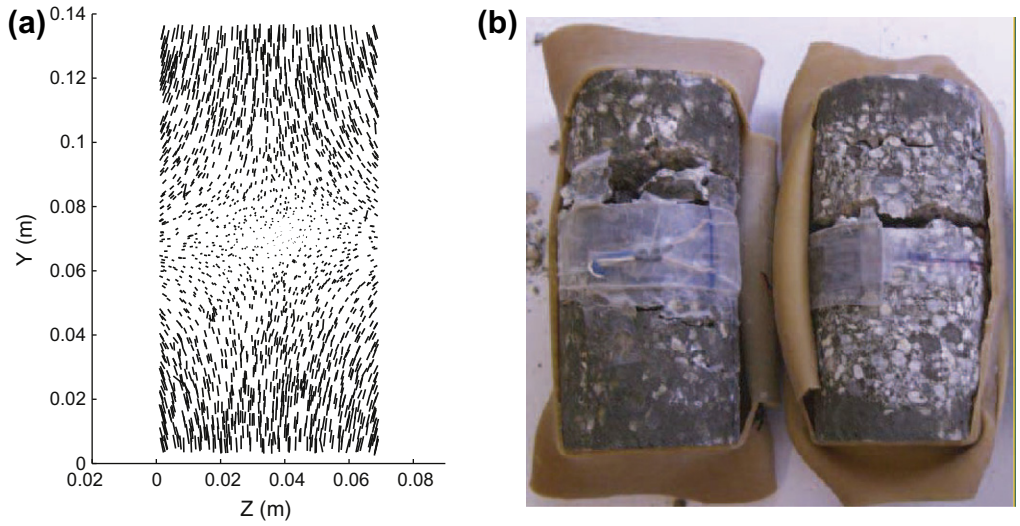

Fig. 23. Displacement field within a thin central vertical slice in the numerical sample during unloading and after the peak stress has been reached in a 650 MPa triaxial test (a) and the fracture topography for a 650 MPa experimental triaxial test (b).

elements is represented when the unloading process starts (see Fig. 23a). The perpendicular orientation of the macro-crack resulting from the coalescence of the broken links is similar to the one observed in the experimental tests (see Fig. 23b).

4.4.3. Discussion

The compaction process results from a coupling between an elastic behavior and two simultaneous irreversible phenomena which are, the collapse of the porosity of the sample and the structural de-cohesion of the cement matrix [13]. When the confining pressure is high, the rearrangement of discrete elements within the numerical model is no longer possible, since the DE cannot be deformed and only overlapping is authorized. Thus, the only way to simulate the compaction process is to control how the overlapping will evolve and this is done by adding the nonlinear hardening step to the compressive part of the interaction forces. The key point is that when using a discrete description of the medium, by simply adding this normal interaction force type, it is possible to get a good macroscopic description (i.e. stress–strain or volumetric curves), as well as the orientation of the compaction process. Since the DE mainly overlap in the main stress direction, when unloading occurs, the tensile limit is reached first for these interactions (see Fig. 5). This induces a perpendicular coalescence of the broken links (which represent the discontinuities in the medium), which leads to an orientation of the macro-cracks comparable to the compaction bands experimentally observed.

5. Conclusion

A Discrete element model using a local elastic-hardening-damage constitutive law has been formulated to reproduce the behavior of concrete at high-confining pressures. In order to get

quantitative results, the model needs to be calibrated first. To do, simulations of uniaxial compression–traction, 650 MPa hydrostatic and 50 MPa triaxial tests are performed to identify the values of the local parameters. As observed, the volumetric behavior can be well reproduced if a coefficient λ, which controls the sliding threshold, is added to the Mohr–Coulomb criterion.

After this calibration step, the model is validated by simulating triaxial tests for different confining pressures (up to 650 MPa), without modifying the local parameter values: here the model is used as a predictive tool. The experimental stress–strain and volumetric curves were well reproduced by the model.

Once these macroscopic comparisons were done, the evolution of the local properties of the model were investigated. It was seen that the evolution of the nature of the local interactions forces could correctly explain the macroscopic response of the sample. For example, the brittle behavior is mainly controlled by a large number of interaction forces in tensile mode, whereas their vanishing corresponds to a ductile transition occurring when the confining pressure increases. Moreover, the compaction process is mainly controlled by the hardening-damage part of the interaction forces in compression. The orientation of the resulting micro-cracks generate discontinuities comparable to the compaction band observed experimentally.

Here, the numerical model does not have a fully microscopic description of the material, since the contribution of the cement matrix is expressed directly in the interaction forces. This is a deliberate choice, in order to be able to simulate large scale structures.

References

[1] Alonso-Marroquin F, Vardoulakis I, Herrmann HJ, Weatherley D, Mora P. Effect of rolling on dissipation in fault gouges. Phys Rev E 2006;74(1):n3.

[2] Bazant Z, Bishop F, Chang T. Confined compression tests of cement paste and concrete up to 300 ksi. ACI J 1986;33:553–60.

[3] Belheine N, Plassiard J-P, Donzé F-V, Darve F, Seridic A. Numerical simulation of drained triaxial test using 3D discrete element modeling. Comput Geotech 2007;36(1-2):320–31.

[4] Burlion N, Gatuingt F, Pijaudier-Cabot G, Daudeville L. Compaction and tensile damage in concrete: constitutive modelling and application to dynamics. Comput Meth Appl Mech Eng 2000;183(3-4):291–308.

[5] Burlion N, Pijaudier-Cabot G, Dahan N. Experimental analysis of compaction of concrete and mortar. Int J Numer Anal Meth Geomech 2001;25:1467–86.

[6] Cundall PA, Hart RD. Numerical modeling of discontinue. Eng Comput 1992;9:101–13.

[7] Cundall PA, Strack OD. A discrete numerical model for granular assemblies. Geotechnique 1979;29:47–65.

[8] Cusatis G, Pelessone D. Mesolevel simulation of reinforced concrete structures under impact loadings. In: Proceedings of the EURO-C 2006 conference on computational modelling of concrete structures, 27–30 March, 2006, Mayrhofen, Tyrol, Austria; 2006.

[9] Donzé F, Magnier SA. Formulation of a three-dimensional numerical model of brittle behavior. Geophys J Int 1995;122:790–802.

[10] Donzé F, Magnier SA, Daudeville L, Mariotti C. Numerical study of compressive behaviour of concrete at high strain rates. J Eng Mech 1999;125(10):1154–63.

[11] Donzé F, Richefeu V, Magnier SA. Advances in Discrete Element Method applied to soil, rock and concrete mechanics. In: State of the art of geotechnical engineering. Electr J Geotech Eng, 2009: 44p.

[12] Gabet T, Vu XH, Malecot Y, Daudeville L. A new experimental technique for the analysis of concrete under high triaxial loading. J de Phys IV 2006;134:635–40.

[13] Gabet T, Malcot Y, Daudeville L. Triaxial behaviour of concrete under high stresses: influence of the loading path on compaction and limit states. Cem Concr Res 2008;38:403–12.

[14] D Hart R, Cundall PA, Lemos J. Formulation of a three-dimensional distinct element model. II: mechanical calculations for motion and interaction of a system composed of many polyhedral blocks. Int J Rock Mech Min Sci Geomech Abstr 1988;25:117–25.

[15] Hentz S, Daudeville L, Donzé FV. Discrete element modelling of concrete submitted to dynamic loading at high strain rate. Comput Struct 2004;82(29–30):2509–24.

[16] Hentz S, Daudeville L, Donzé FV. Identification validation of a discrete element model for concrete. J Eng Mech, ASCE 2004;130(6):709–19.

[17] Iwashita K, Oda M. Micro-deformation mechanism of shear banding process based on modified distinct element method. Powder Technol 2000;109:192–205.

[18] Jamet P, Millard A, Nahas G. Triaxial behaviour of a micro concrete complete stress strain for confining pressures ranging from 0 to 100 MPa. In: International conference on concrete under multiaxial conditions, vol. 1. INSA Toulouse (France): Presses de lUniversit Paul Sabatier; 1984. p. 133–140.

[19] Kozicki J, Donzé FV. Applying an open-source software for numerical simulations using finite element or discrete modelling methods. Comput Meth Appl Mech Eng 2008;197(49-50):4429–43.

[20] Kozicki J, Donzé FV. YADE-OPEN DEM: an open-source software using a discrete element method to simulate granular material. Eng Comput 2009;26(7):786–805.

[21] Li H, Pugh D. Mechanical behaviour of materials under pressure. Elsevier; 1970.

[22] Plassiard JP, Belheine N, Donzé FV. A spherical discrete element model: calibration procedure and incremental response. Granul Matter 2009;11(5):293–306.

[23] Potyondy D, Cundall PA. A bonded-particle model for rock. Int J Rock Mech Min Sci 2004;41:1329–64.

[24] Rousseau J, Frangin E, Marin P, Daudeville L. Damage prediction in the vicinity of an impact on concrete structure : a combined FEM/DEM approach. Comput Concr 2008;5(4):343–58.

[25] Schmidt JM. High pressure and high strain rate behaviour of cementitious materials: experiments and elastic/viscoplastic modeling. PhD thesis, University of Florida, USA; 2003.

[26] Shiu W, Donzé FV, Daudeville L. Compaction process in concrete during missile impact: a DEM analysis. Comput Concr 2008;5(4):329–42.

[27] Shiu W, Donzé FV, Daudeville L. Influence of the reinforcement on penetration and perforation of concrete targets: a discrete element analysis. Eng Comput 2009;26(1):29–45.

[28] Vu XH, Malecot Y, Daudeville L, Buzaud E. Experimental analysis of concrete behavior under high confinement: effect of the saturation ratio. Int J Solids Struct 2009;46:1105–20.

[29] Wang Y, Mora P. Macroscopic elastic properties of regular lattices. J Mech Phys Solids 2008;56(12):3459–74.

[30] Warren T, Fossum A, Frew D . Penetration into low-strength (23 MPa) concrete: target characterization and simulations. Int J Impact Eng 2004;30:477–503.